Research article

Nanomechanical inhomogeneities in CVA-deposited titanium nitride thin films: Nanoindentation and finite element method investigations

Neeraj Kumar Sharma, Anchal Rana, O.S. Panwar, Abhimanyu Singh Rana [*]

Centre for Advanced Materials and Devices, School of Engineering and Technology, BML Munjal University, Sidhrawali, Gurugram, 122413, Haryana, India

A B S T R A C T

Refractory metals that can withstand at high temperatures and harsh conditions are of utmost importance for solar-thermal and energy storage applications. Thin films of TiN have been deposited using cathodic vacuum arc deposition at relatively low temperatures ~300 °C using the substrate bias ~ −60 V. The nanomechanical properties of these films were investigated using nanoindentation and the spatial fluctuations were observed. The nanoindentation results were simulated using finite element method through Johnson-Cook model. A parametric study was conducted, and 16 different models were simulated to predict the hardening modulus, hardening exponent, and yield stress of the deposited film. The predicted values of elastic modulus, yield stress, hardening modulus and hardening exponent as 246 GPa, 2500 MPa, 25000 MPa and 0.1 respectively are found to satisfactorily explain the experimental load-indentation curves. We have found the local nitridation plays an important role on nanomechanical properties of TiN thin films and confirms that the nitrogen deficient regions are ductile with low yield stress and hardening modulus. This study further opens the opportunities of modelling the nanoscale system using FEM analysis.

1. Introduction

There are not many refractory materials with both metallic and plasmonic characters that are suitable for thermo-photovoltaics and solar-thermal applications and that can replace the precious metals like silver and gold [1–8]. There is a renewed interest in titanium nitride (TiN) as a plasmonic metamaterial [4,9–12] as a cathode material for energy storage [13–16] and catalysis [17–22]. The nanomechanical properties, surface defects and stoichiometry are crucial for the overall device functionality and reliability [5,6, 23–27]. Vacuum-based physical vapor deposition (PVD) techniques such as sputtering [28,29], high-power impulse magnetron sputtering [24], pulsed laser deposition [30,31], and cathodic vacuum arc (CVA) deposition [32] have been widely used for synthesizing the TiN thin films. However, measuring the local properties of metal-nitrides is a daunting task as the inert nature of the nitrogen molecules and the undesirable formation of oxides can lead to nanoscopic inhomogeneities in mechanical properties [33–35]. The nanoindentation technique can be a promising method to investigate the nanomechanical properties [36]. The advantage of nanoindentation compared to the tensile test is that the elastic modulus, hardness and flow stresses can be evaluated without the
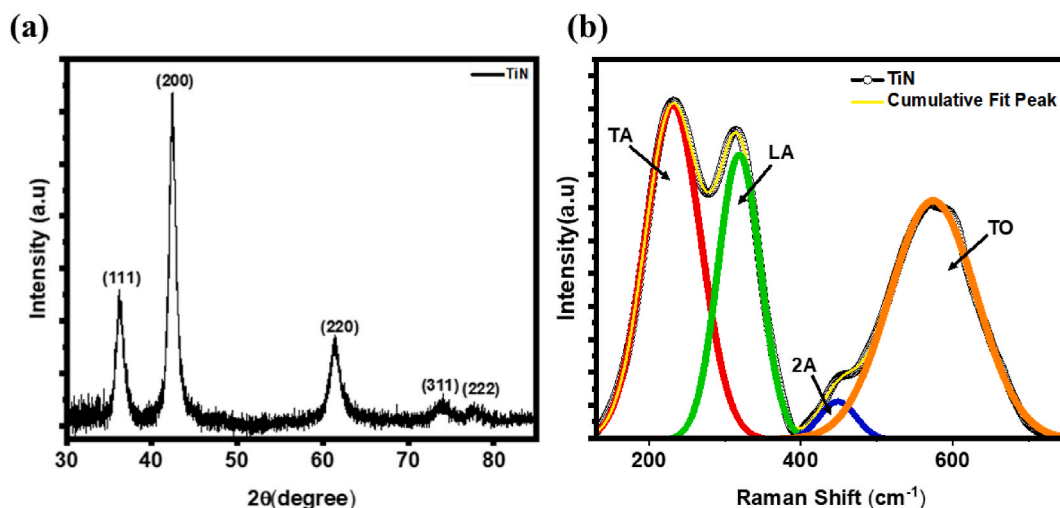

Fig. 1. (a) X-ray diffraction (XRD) and (b) Raman spectroscopy results of CVA-deposited TiN thin films.

standard specimen fabrication. It is generally suggested that for hardness measurement, the maximum indentation depth should be within 10 % of film thickness, however, at such elastic modulus measurement may be subjected to error due to the significant indenter tip radius at low depth [37,38]. The indentation depth is kept at lower values in order to ensure that there is no contribution from substrate in the measured data. Finite element method (FEM) can be advantageous in this situation for the back analysis of the experimental results and to obtain the coated material parameters. Some of the authors have used FEM to generate the load-depth curves and the inverse analysis has been performed using artificial neural network [39–41].Lee et al. have used the FE modelling for nanoindentation simulation. An axis symmetric model with pressure dependent material behavior using Drucker-Prager yield criterion was used to predict the thin film metallic glass properties [37]. Peng. et al. have conducted FE analysis for a large range of elasto-plastic materials and the yield strength and hardening exponent was predicted based on an energy-based combined dual-conical indentation model [42].

In this work, the titanium nitride (TiN) thin films grown by CVA deposition have been investigated using the nanoindentation to understand the nanomechanical properties of titanium nitride (TiN). The previously reported work on TiN thin film has not been studied using numerical techniques such as FEM, in order to understand effects of the experimental parameters. A total number of 16 different material models have been studied using Johnson-Cook plasticity behaviour using FE analysis to understand the effects of experimental parameters on the deposited film. The yield stress, strain hardening coefficient and the strain hardening exponent have been predicted using the FE analysis.

2. Experimental

Titanium nitride (TiN) thin films of were deposited using cathodic vacuum arc on 7059 glass and silicon substrates by evaporating a ~99.999 % pure titanium metal target (75 mm diameter) producing an arc current of ~150–160 A at −50 V bias, in the presence of background nitrogen gas having pressure ranging from $\sim 1 \times 10^{-4}$ mbar to $\sim 1 \times 10^{-3}$ mbar. The substrate was biased at ~60 V and heated at temperature of ~200–300 °C during the deposition. Prior to the deposition, a base pressure better than 5×10^{-6} mbar was achieved. Prior to the deposition, a base pressure better than 5×10^{-6} mbar was achieved, and the substrates were cleaned *in-situ* using the argon gas plasma for 5 min at the DC bias voltage ~ - 460 V. The perpendicular distance from the cathode (target) to the anode was ~250 mm. The sum of the bias voltage and the incident ion energy of the Ti constitute the incident ion energy. The crystal structure of the films was confirmed by X-ray diffraction (XRD) by Panalytical and Raman spectroscopy by Witec (Alpha 300) system. Raman spectra were acquired using a green laser (532 nm) with a ~5 mW incident power. The chemical composition and stoichiometry of these films were confirmed by X-ray photoelectron spectroscopy (XPS) using Thermo Fisher (k Alpha) system. The commercial IBIS nanoindentation from Fischer-Cripps Laboratories Pvt. Ltd., Australia was used to acquire load – displacement curves having a standard triangular pyramid diamond Berkovich indenter with a normal angle of 65.27° and tip radius of ~100 nm). The linear variable of differential transformers (LVDT) sensors was used to record the force and depth measurements The fused silica and sapphire are used as standard specimens are used to verify the operation of the instrument before the performing the measurements on sample. The surface was analysed by the scanning electron microscope by Hitachi (SU3500). Thickness and the roughness of these thin films were measured by surface profilometer by Brucker, Dektak XT.

3. Results and discussion

X-ray diffraction can be seen in Fig. 1 (a), showing sharp peaks at ~36.2°, 42.3°, and 61.27° related to (111), (200), and (220) crystalline planes, respectively. This matches with the TiN cubic structure. However, the peaks around 74° and 77.8° related to (311)
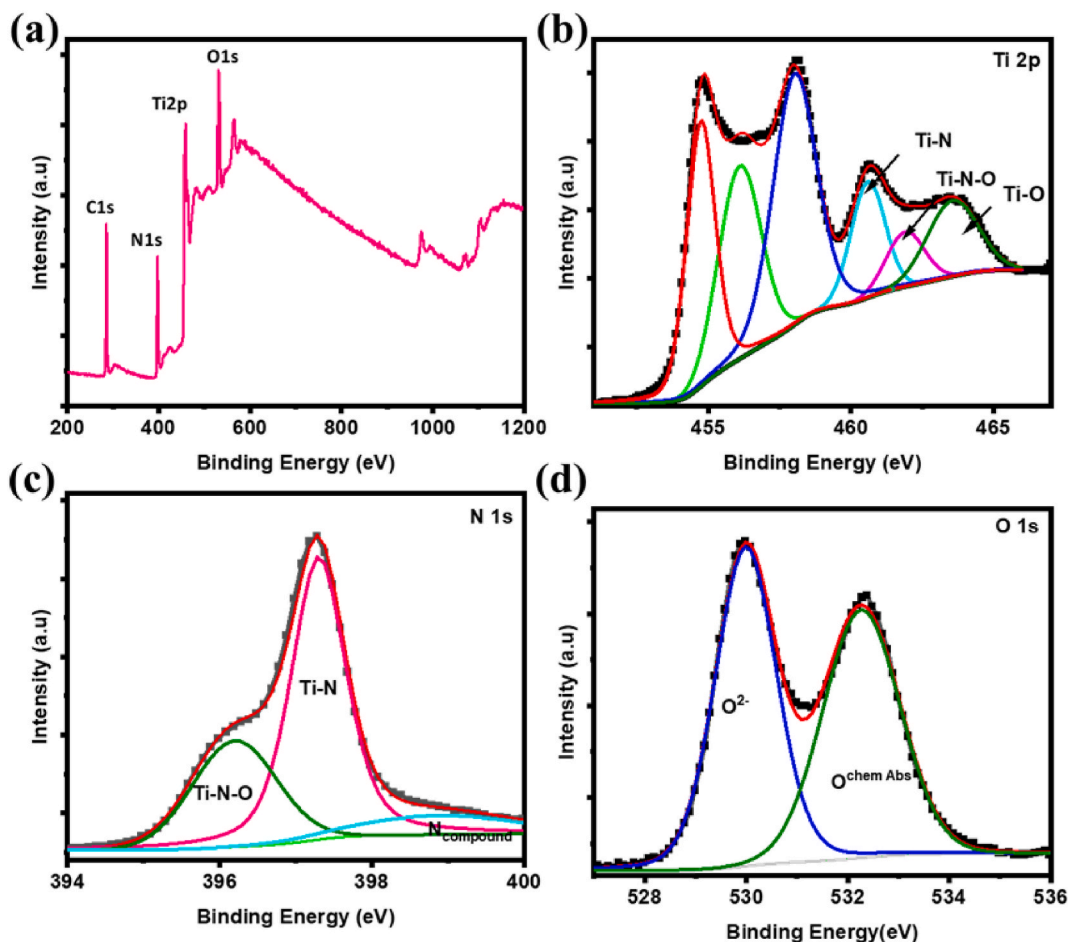
Fig. 2. X-ray photoelectron spectroscopy results of CVA-deposited TiN thin films. (a) The full scan, (b) the Titanium (Ti) 2p orbital binding energy peaks (c,d) Nitrogen (N) and Oxygen (O) 1s orbital binding energy peaks.

and (222) planes are slightly shifted to a higher angle due to compressive strain originated due to the lattice mismatch between pure TiN and Ti metal clusters caused by nitrogen vacancies [43].

Also, TiN is one of the transition metal nitrides that does not show first-order Raman scattering due to O_h symmetry. But the presence of defects (or vacancies) within the lattice induces Raman scattering. We also observed the Raman peaks in these films as shown in Fig. 1 (b). The Raman spectroscopy was performed at a low laser power of 5 mW to avoid the formation oxide locally. The Gaussian fitted curves are shown in Fig. 1 (b), where he first-order phonon peaks around $\sim$ 230 cm^{-1}, 318 cm^{-1}, 568 cm^{-1}, and 665 cm^{-1} can be seen for transverse acoustic (TA), longitudinal acoustic (LA), transverse optical (TO), and longitudinal optical (LO) modes of cubic nanocrystalline TiN respectively [44]. On the other hand, the peak 448 cm^{-1} is the second-order acoustic phonon mode. The first-order acoustic modes are mainly caused by the Ti–Ti atoms vibrations in the presence of N vacancies. The optical phonon modes, on the other hand, are due to the N–N atoms adjacent to Ti vacancies. Therefore, the presence of both modes confirms the stochiometric inhomogeneities in TiN lattice.

Along with the structural information obtained by XRD and Raman spectroscopy, it is interesting to see the surface chemical composition of these films. Fig. 2 shows X-ray photoelectron (XPS) spectra of these films. The XPS full scan spectra in Fig. 2 (a) clearly confirms the presence of Ti 2p, N 1s, O1s, and C1s peaks of core energy levels. The fitting and raw XPS spectra are shown in Fig. 2(b–d). The titanium (Ti 2p) orbital of TiN shows several peaks, corresponding to different Ti bonding. The binding energy peak at 454.78 eV ($p_{3/2}$) and 460 eV ($p_{1/2}$) indicates the presence of Ti–N bonds. Apparently, the oxygen in the TiN film is also seen due to the formation of thin layer of oxynitride on the surface [7]. The formation of the oxide layer gives rise to the peaks at 458.18 eV ($p_{3/2}$) and 463.78 eV ($p_{1/2}$), which indicates the presence of Ti^{4+} and the formation of TiO$_2$. The peak between these two at 456.38 eV($p_{3/2}$) and 462.38 eV ($p_{1/2}$) indicates the formation of an intermediate state of TiO$_2$ and TiN i.e, titanium oxynitride (TiN$_x$O$_y$). In the N(1s) spectrum, peaks were observed at 396.3 eV, 397.2 eV, and 398.5 eV. The highest peak is attributed to the TiN phase, while the other two peaks correspond to TiN$_x$O$_y$ and nitrogen compounds, respectively. The 1s Oxygen shows two peaks at 529.9 eV and 532.2 eV attributed to O^{2+} and chemically absorbed oxygen (O$^{chem\ Abs}$) on the surface of TiN.
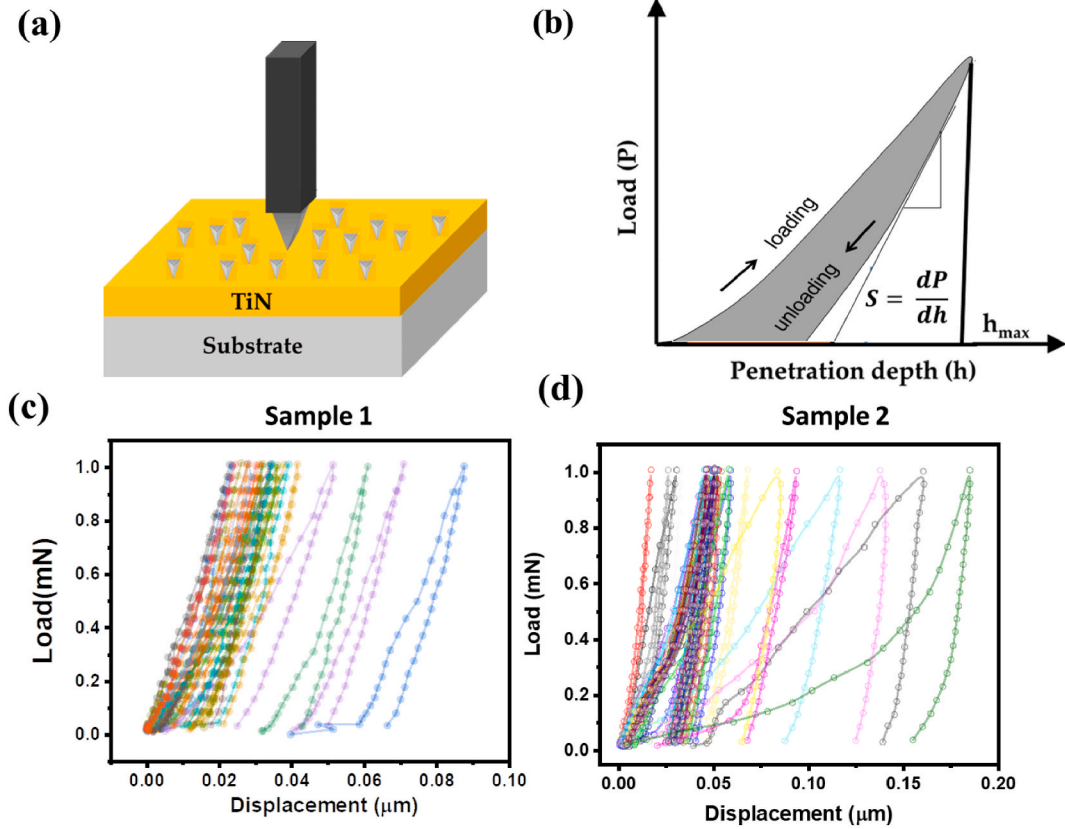
Fig. 3. (a) Schematic of nanoindentation performed on TiN thin films. (b) Schematic of typical load-displacement curve. (c–d) The nanoindentation curves obtained at different locations of TiN films grown under nitrogen background pressures of $\sim 1 \times 10^{-3}$ mbar (c) and $\sim 1 \times 10^{-4}$ mbar (d).
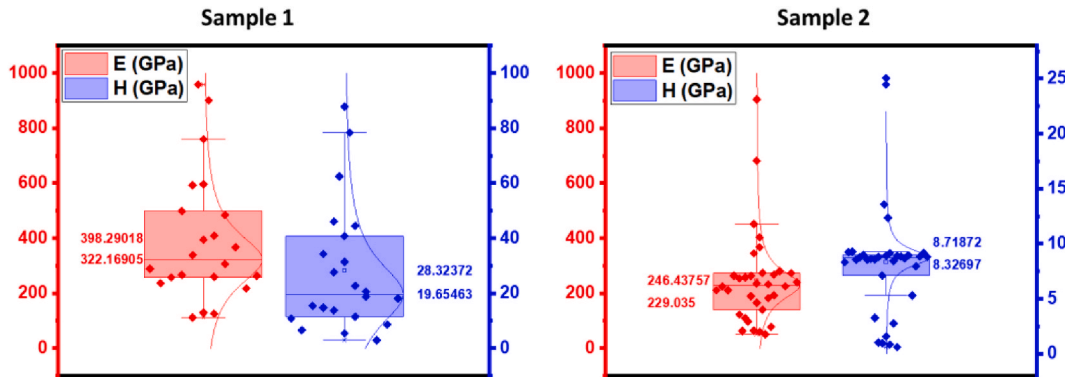

Fig. 4. The statistical distribution of elastic modulus (E) and hardness (H) values of TiN grown under nitrogen background pressures of (a) $\sim 1 \times 10^{-3}$ and (b) $\sim 1 \times 10^{-4}$ mbar.
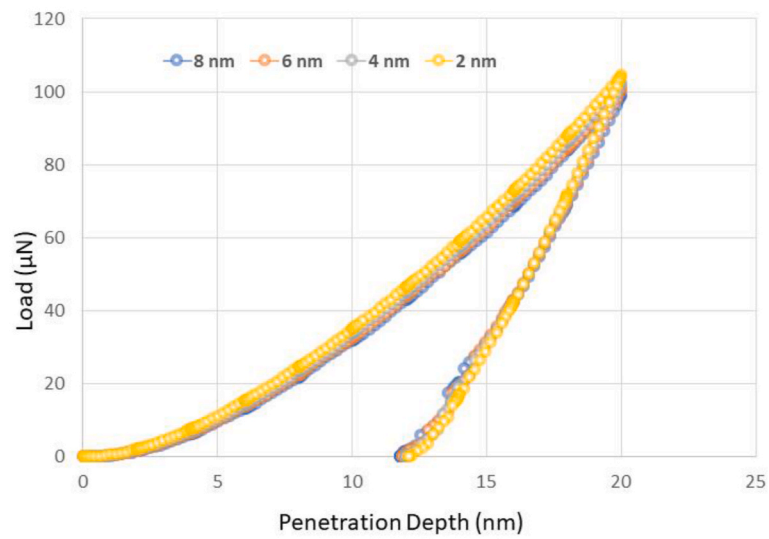
3.1. Nanoindentation analysis

Therefore, it would be interesting to see how these surface defects influences the nanomechanical properties locally. Fig. 3 (a) and 3 (b) illustrate the schematics of the nanoindentation measurement set-up and the typical load versus indent penetration depth to measure the hardness and elastic modulus at nanoscale, which is very similar to the Vickers hardness tester used for measuring microscopic hardness values. In nanoindentation, however, the contact area is estimated by measuring the penetration depth of the indenter into the sample using the diamond indenter tip of known geometry [45]. For the Berkovich indenter tip, the projected contact area $A = 3\sqrt{3}\, h^2\, tan^2\, \theta$, where h is the penetration depth and the angle θ is $\sim 65.27°$ between the tip axis and the faces of the triangular pyramid of the Berkovich indenter, giving $A = 24.5\, h^2$. The hardness and elastic modulus can be calculated [45] using the expressions
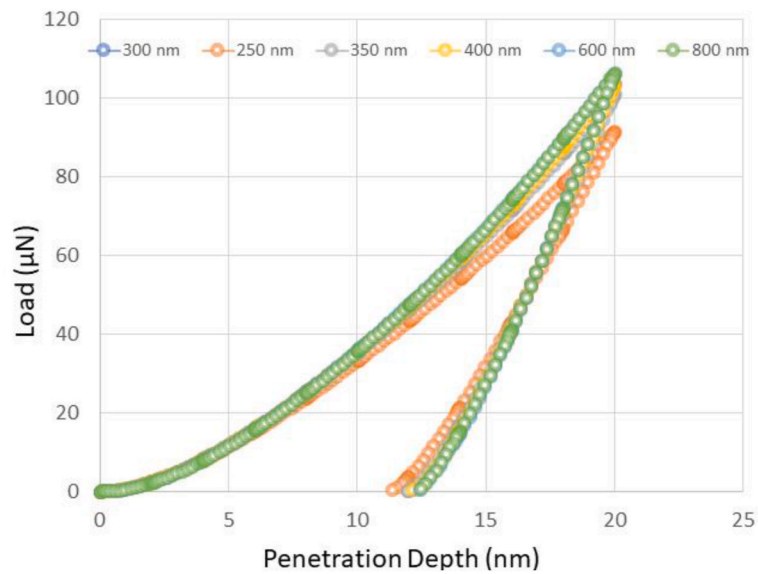
(a)
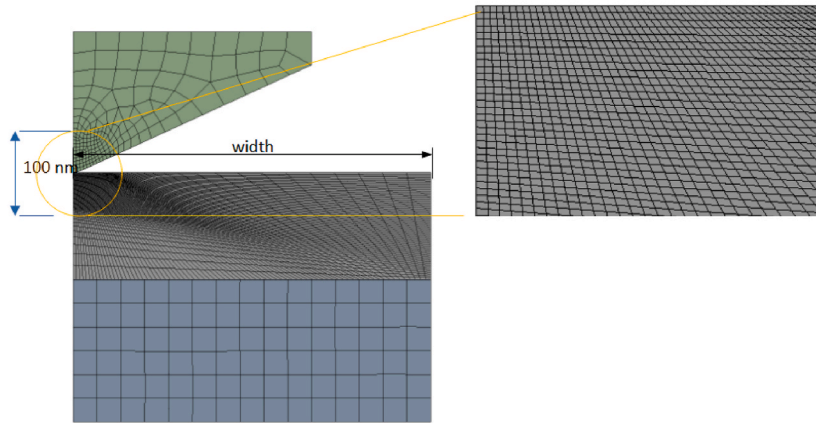
(b)

(c)

Fig. 5. (a) Two-dimensional axis symmetric model for nanoindentation. (b) Convergence study for different mesh element size (nm); (c) RVE sensitivity analysis.

Table 1

Mechanical properties of the materials used in the finite element model.

	Elastic Modulus (GPa)	Poisson's ratio	Yield Stress (MPa)	Hardening exponent	Hardening modulus (MPa)
Glass	75	0.23	–	–	–
Diamond	1141	0.07	–	–	–
TiN	246	0.25			

$H = P/24.5h^2$ and $E = 1/\beta\sqrt{\pi}/2 \ S/\sqrt{A}$, where β is a constant of ~1.034 for the Berkovich indenter and S is the stiffness obtained from the slope of the load-displacement curve as illustrated in Fig. 3 (b) The tip was calibrated using the standard substrates with varying load in the range 1–4 mN and the results presented are at the lowest load available in the instrument. Fig. 3 (c) and 3 (d) shows the nanoindentation measurements on CVA-deposited TiN thin films grown under nitrogen background pressures of $\sim 1 \times 10^{-3}$ mbar and $\sim 1 \times 10^{-4}$ mbar, respectively. The nanoindentation curves are obtained at different locations on surface the results are shown in Fig. 3 (c). It can be observed from these graphs that there is a large spatial variation in the indentation penetration depth (h) can be seen Nitrogen deficient samples. Also, the statistical distribution of elastic modulus (E) and hardness (H) values of nitrogen rich and deficient samples are shown in Fig. 4 (a) and 4 (b) respectively which shows a clear reduction in the median and mean values E and H in nitrogen deficient samples.

Since it was not possible to physically see the indent made by nanoindentation method. We have attempted to make indent using the atomic force microscope (AFM) having diamond coated tips. To acquire the force-distance (F-D) graphs, as shown in figure S1 (a-b), an AFM tip is brought ~ 1 μm far away from the film surface where there is no interaction with the tip and then pushed against the surface and then finally retracted back to the original position with concurrent recording of the bending of the cantilever (measured as deflection on a detector). Note that the slope in F-D graph does not provide any explicit information about the sample mechanical properties but rather dominated by the spring constant of the cantilever. However, if indentation does occur it will show the hysteresis and a slight change in the slope in the F-D curve. It is interesting to note when the F-D measurement is performed and subsequently the same area is imaged with contact mode AFM, a hysteresis and a clear indent can be seen in the films grown under nitrogen deficient conditions. It was not possible to precisely calculate the hardness value from the penetration depth of AFM tip ~150 nm, but our estimated hardness value of ~2 GPa agrees nanoindentation measurements, considering the applied load (1 V ~ 6300 nN) by AFM divided by the area of the impression (~170 nm^2) taken from the topographic AFM image [also correlated with SEM image of commercial tip in figure S1 (C)]. Thus, these results confirm that the nanomechanical properties are influenced by the local changes in the nitriding process of these films.

3.2. Finite element analysis

Finite element method has been used for the back analysis of the nanoindentation testing data to obtain the coated material parameters. The real and more complex 3D model was reduced to an axisymmetric 2D model since the model is symmetric with respect to geometry, properties and the loading conditions. This simplifies the analysis procedure, accelerate the back analysis nanoindentation process and reduces the computational cost. The previously reported work also approves that the 2D results matches well with the 3D results for Berkovich indenter [46–48]. The glass substrate of rectangular domain of 400 nm thickness having a 300 nm thick titanium nitride thin film over the surface of glass substrate was modelled, as the geometry shown in Fig. 5 (a). In order to decide the suitable width for axisymmetric analysis, representative volume element (RVE) of thin film coated glass surface having a width varying from 250 nm to 1000 nm were generated and a parametric analysis was conducted. The top surface of the thin film was in contact with the indenter having a normal angle of 65.3° and a tip radius of 100 nm. The thin film and the substrate were assumed to be perfectly bonded. A frictionless contact between the indenter and the TiN film was assumed considering the hardness of indenter [49]. The quadrangular shaped second-order elements were used to mesh the geometry. A very fine mesh near the tip of the indenter and around the contact region was created. The FEA solver in ANSYS used full Newton-Raphson method for nonlinear control. The step size was kept very small varying from 1e-06 to 0.1 to obtain the convergence. The large deflection was allowed to accurately model the nonlinear deformation during simulation.

The TiN film was modelled as the elastoplastic material with elastic modulus (E) same as predicted from experiments, 246 GPa for CVA deposited film. The plastic deformation of TiN film, was modelled using the Johnson-Cook model in which the flow stress, σ and the equivalent plastic strain, ε are related as:

$$\sigma = (A + B\varepsilon^n)(1 + C ln\dot{\varepsilon}^*)(1 - T^{*m}) \tag{1}$$

where *A, B, n, C,* and *m* are material constants. A, *B* and n are known as yield stress (σ_y), hardening modulus and work-hardening exponent, respectively. *C* and *m* are the strain rate hardening and thermal softening coefficient, respectively. For quasistatic conditions with no temperature change, C = 0, T* = 0. Hence, the final relation is reduced to:

$$\sigma = B\left[\sigma_y + \left(\frac{\sigma_y}{E}\right)^n\right] \tag{2}$$

The glass substrate and the diamond indenter were modelled as linear elastic material (see Table 1). A frictionless support was applied at the axis of symmetry and the substrate base was constrained by fixed displacement. The indenter was assigned a

Table 2
Material parameters used for FE simulations for coated TiN film.

Model	Elastic Modulus (GPa)	Yield Stress (σ_y) (MPa)	Hardening modulus B (Mpa)	Hardening exponent, n
model 1	246	1500	2000	0.5
model 2		1500	2000	0.1
model 3		1500	1500	0.5
model 4		1000	1500	0.5
model 5		2500	1500	0.1
model 6		2500	6000	0.1
model 7		3500	10000	0.1
model 8		3500	15000	0.1
model 9	400	3500	10000	0.1
model 10	200	1500	2000	0.5
model 11	200	1000	1500	0.5
model 12	246	600	1000	0.5
model 13		4500	10000	0.1
model 14		2500	25000	0.1
model 15		2500	30000	0.1
model 16		2500	25000	0.2

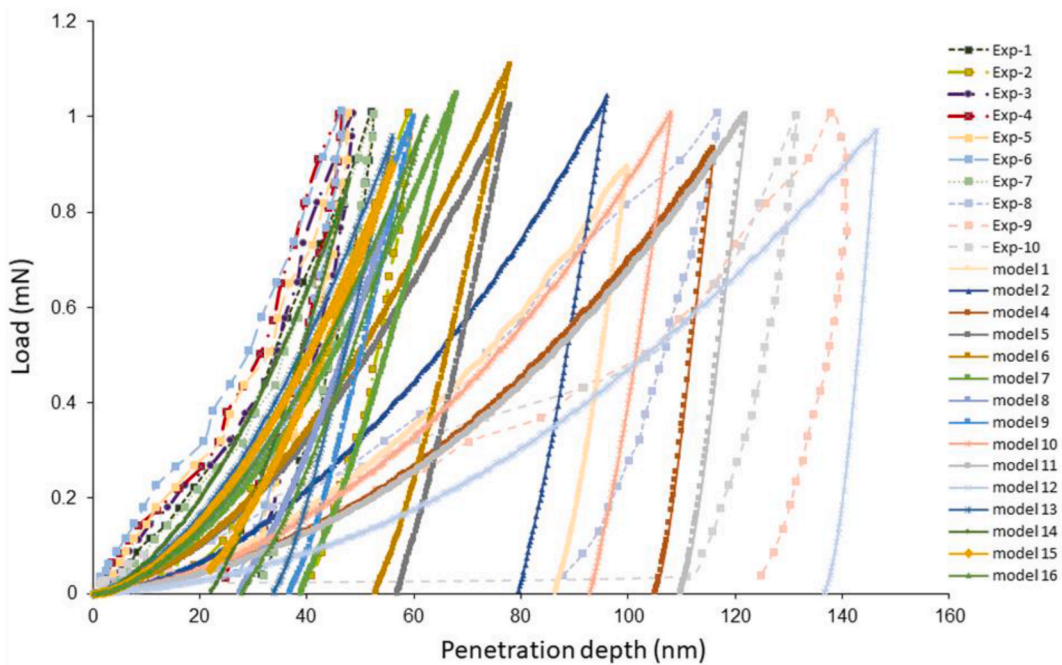**Fig. 6.** Nanoindentation curves resulted from FEM analysis for CVA deposited coating with 16 different models with 600 MPa $\leq \sigma_y \leq$ 3500 MPa and $0.1 \leq n \leq 0.5$.

displacement boundary condition in a multistep analysis with 2 nm of vertical displacement in each step for loading and unloading conditions. The previously reported work suggest that the yield stress is 1/100th of elastic modulus, and the strain hardening exponent for most of metals is considered between 0 and 0.5. A parametric analysis with the assumed values of the hardening modulus and the exponent has been conducted and the simulated nanoindentation curves were compared with the experimental values. The properties used for simulation are mentioned in Table 2.

Fig. 5 (b) shows the load-indentation curves for different mesh element size varying from 8 nm to 2 nm. This element size was varied for the 100 nm highlighted region near to the tip of the indenter, considering this to be a high stress concentration zone, as shown in Fig. 5 (a). As the mesh element size reduces, the number of mesh element increases and hence the computational cost. For 2 nm, mesh element size, it results into a total of 5066 quadrangular second-order elements with 15575 number of nodes. The element quality was also measured using mesh metric 'Element Quality' and it was measured to be a minimum of 0.10179 and an average of 0.557.

It can be observed that the load-indentation curves are sensitive to the mesh size and as the element size reduces the results got converged. For 2 nm maximum element size, the simulated load values differ within 2 % in the peak load region and therefore this element size is used as the default element length in all simulations. In can also be observed in Fig. 5 (c) that the width of RVE has a
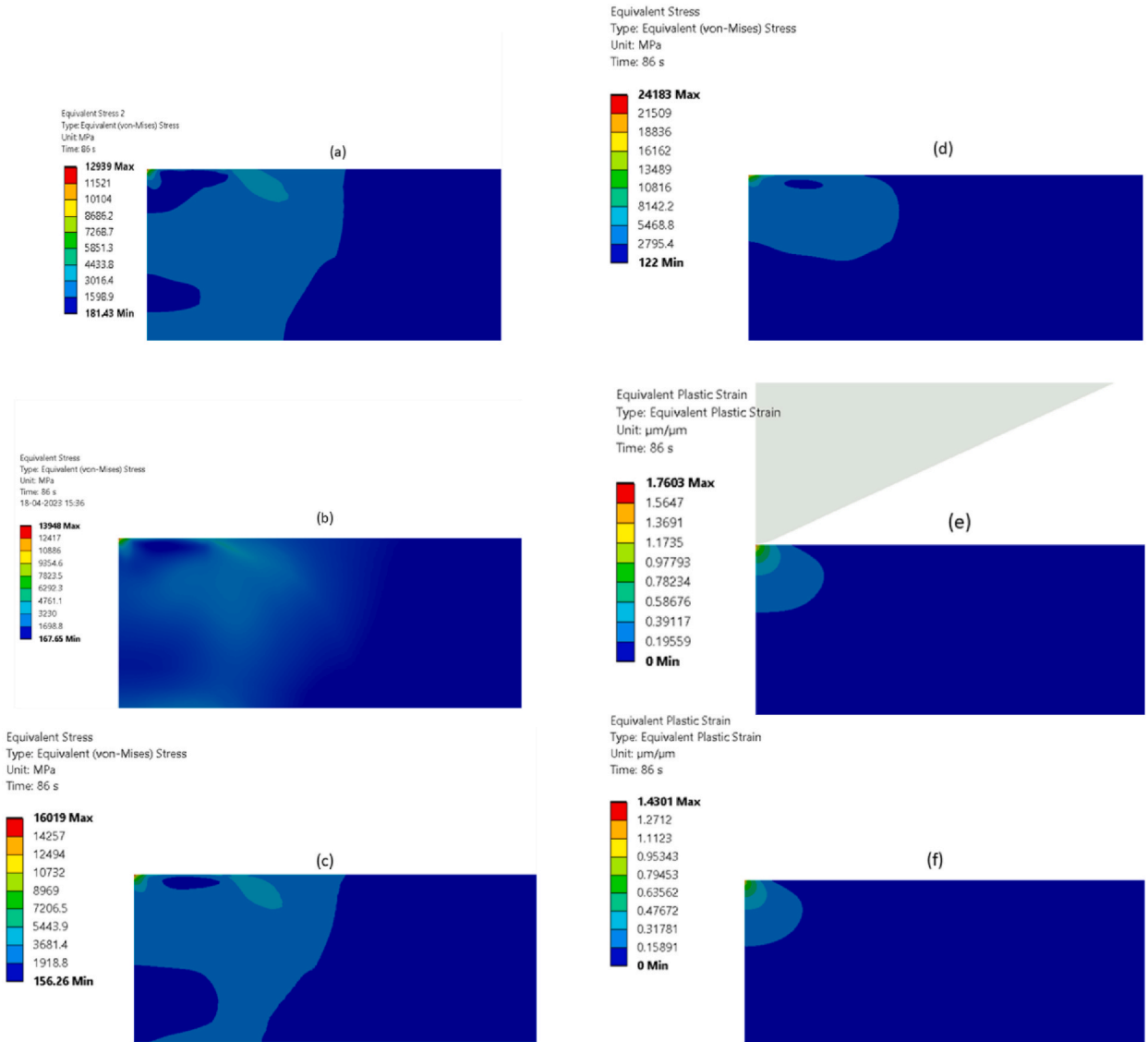
Fig. 7. von- Mises stress (MPa) contours for TiN thin film (a) model 3, (b) model 5, (c) model 6, (d) model 7, (e) Equivalent Plastic strain model 6, (f) equivalent plastic strain model 7.

considerable effect on the load-indentation curves for the 2D axisymmetric modelling. As the RVE width increases more than 400 nm, the predicted load values start converging. Therefore, for all simulation models in this paper, a width of 1000 nm has been considered.

Fig. 6 shows the simulated load-indentation curves for 16 different models. The simulated curves are compared with the experimental curves obtained in case of CVA deposited coating. It can be observed that the indentation depth increases as the yield stress and hardening modulus reduces. In case of model 12, the yield stress and hardening modulus are 600 MPa and 1000 MPa respectively, that results into a 146 nm indentation at a peak load of 0.972 mN. A lower value of yield stress initiates plastic deformation earlier. The strain hardening behaviour of the coated material depends on the hardening modulus and the hardening exponent. Therefore, the lower values of hardening modulus results into increased plastic strain. Another observation that can be made from the simulated plots is that the lower values of hardening exponent results into high values of flow stresses and therefore more load and less indentation depth. The experimental plots for Exp-8 to 10, are best represented by FEA model-11 and model-12. The high penetration depth in case of experiments 8–10 shows that the coating in that region is more ductile with low yield stress in between 600 and 1000 MPa, hardening modulus in between 1000 and 1500 MPa and hardening exponent 0.1. This, further supports our previous conclusions from experiments that the region of CVA deposited film is grown under nitrogen deficient conditions leading to more ductile behaviour. A clustering of experimental curves can be observed in the region with penetrating depth less than 40 nm. This low penetration depth curves are best represented by models having yield stress around 2500 MPa and a high hardening modulus close to 25000 MPa.

Fig. 7(a–d) shows the von-Mises stress for four different models: model 3, model 5, model 6 and model 7. The stress concentration
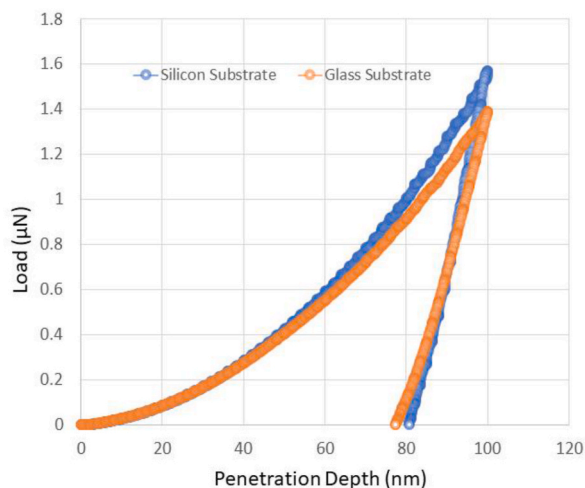
Fig. 8. Nanoindentation curve for glass and silicon substrate for model 4.

increases as the yield stress increases. Model 3 has a yield stress of 1500 MPa and hence the plastic deformation starts earlier comparing to the model 7 which has a yield stress of 3500 MPa. A higher value of equivalent plastic strain for model 6 [Fig. 6 (e)] comparing to model 7 [Fig. 7 (f)] is due to a lower value of yield stress for model 6.

In order to understand the effects of substrate, the nanoindentation simulations of TiN thin film coated on glass and silicon substrate are compared in Fig. 8. It can be seen from the nanoindentation curves that the elastic modulus of both the curves are same, however the hardening coefficient of silicon substrate deposited TiN film is slightly higher than that of glass substrate deposited TiN film. The strain hardening behaviour post yielding depends on the dislocations movement and grain boundaries formation, which is affected by the interface of thin film and substrate and a soft substrate like silicon results high hardening modulus.

4. Conclusion

In conclusion, the nanoscale spatial inhomogeneity in mechanical properties of TiN thin films were investigated using nano-indentation and atomic force microscopy and spectroscopy. The local nanoindentation load versus penetration depth graphs were simulated using finite element method (FEM). 16 different material models are simulated using FEM by considering different values of hardening modulus, exponent and yield stress. The simulated load-indentation plots were compared with the experimental plots and the material parameters were determined. The experimentally concluded nitrogen deficient nanoindentation plots from certain regions of deposited film were further validated from the FEM simulated material parameters since a lower values of yield stress, hardening modulus has been obtained for such plots. This investigation further opens the new opportunities of modelling the nanoscale system using FEM analysis and predict the nanoindentation results.

Data availability

All data generated or analysed during this study are included in this published article and its supplementary information files.

CRediT authorship contribution statement

Neeraj Kumar Sharma: Writing – review & editing, Writing – original draft, Supervision, Software, Methodology, Investigation, Formal analysis, Conceptualization. **Anchal Rana:** Writing – original draft, Visualization, Software, Methodology, Investigation, Formal analysis. **O.S. Panwar:** Writing – original draft, Methodology, Investigation. **Abhimanyu Singh Rana:** Writing – review & editing, Writing – original draft, Supervision, Project administration, Methodology, Investigation, Conceptualization.

Declaration of competing interest

The authors declare that they have no known competing financial interests or personal relationships that could have appeared to influence the work reported in this paper.

Acknowledgements

Appendix A. Supplementary data

Supplementary data to this article can be found online at https://doi.org/10.1016/j.heliyon.2024.e33239.

References

[1] G.V. Naik, V.M. Shalaev, A. Boltasseva, Alternative plasmonic materials: beyond gold and silver, Adv. Mater. 25 (2013) 3264.
[2] U. Guler, V.M. Shalaev, A. Boltasseva, Nanoparticle plasmonics: going practical with transition metal nitrides, Mater. Today 18 (2015) 227.
[3] U. Guler, A. Boltasseva, V.M. Shalaev, Refractory plasmonics, Science 344 (2014) 263, 1979.
[4] A. Boltasseva, H.A. Atwater, Low-loss plasmonic metamaterials, Science 331 (2011) 290, 1979.
[5] Q. Guo, T. Wang, Y. Ren, Y. Ran, C. Gao, H. Lu, Z. Jiang, Z. Wang, Plasmonic properties of nonstoichiometric zirconium nitride, oxynitride thin films, and their bilayer structures, Phys. Rev. Mater. 5 (2021) 65201.
[6] A. Catellani, P. D'Amico, A. Calzolari, Tailoring the plasmonic properties of metals: the case of substoichiometric titanium nitride, Phys. Rev. Mater. 4 (2020) 15201.
[7] C.-C. Chang, J. Nogan, Z.-P. Yang, W.J.M. Kort-Kamp, W. Ross, T.S. Luk, D.A.R. Dalvit, A.K. Azad, H.-T. Chen, Highly plasmonic titanium nitride by room-temperature sputtering, Sci. Rep. 9 (2019) 15287.
[8] P. Jalili, S. Ghadiri Alamdari, B. Jalili, A. Shateri, D.D. Ganji, Analytical and numerical investigation of heat transfer of porous fin in a local thermal non-equilibrium state, Heliyon 10 (2024) e26424.
[9] Z.Y. Yang, S. Ishii, A.T. Doan, S.L. Shinde, T.D. Dao, Y.P. Lo, K.P. Chen, T. Nagao, Narrow-band thermal emitter with titanium nitride thin film demonstrating high temperature stability, Adv. Opt. Mater. 8 (2020) 1.
[10] W. Li, U. Guler, N. Kinsey, G.V. Naik, A. Boltasseva, J. Guan, V.M. Shalaev, A.V. Kildishev, Refractory plasmonics with titanium nitride: broadband, Adv. Mater. 26 (2014) 7959.
[11] P. Yu, L.V. Besteiro, Y. Huang, J. Wu, L. Fu, H.H. Tan, C. Jagadish, G.P. Wiederrecht, A.O. Govorov, Z. Wang, Broadband metamaterial absorbers, Adv. Opt. Mater. 7 (2019) 1.
[12] T. Ameri, P. Khoram, J. Min, C.J. Brabec, Organic ternary solar cells: a review, Adv. Mater. 25 (2013) 4245.
[13] H. Wang, J. Li, K. Li, Y. Lin, J. Chen, L. Gao, V. Nicolosi, X. Xiao, J.M. Lee, Transition metal nitrides for electrochemical energy applications, Chem. Soc. Rev. 50 (2021) 1354.
[14] B.G. Kim, C. Jo, J. Shin, Y. Mun, J. Lee, J.W. Choi, Ordered mesoporous titanium nitride as a promising carbon-free cathode for aprotic lithium-oxygen batteries, ACS Nano 11 (2017) 1736.
[15] X. Lu, G. Wang, T. Zhai, M. Yu, S. Xie, Y. Ling, C. Liang, Y. Tong, Y. Li, Stabilized TiN nanowire arrays for high-performance and flexible supercapacitors, Nano Lett. 12 (2012) 5376.
[16] S. Yadav, A. Sharma, A. Devi, A. Rana, Electrochimica acta crystalline flower-like nickel cobaltite nanosheets coated with amorphous titanium nitride layer as binder-free electrodes for supercapacitor application, Electrochim. Acta 437 (2023) 141526.
[17] G.S. Shanker, R. Bhosale, S. Ogale, A. Nag, 2D nanocomposite of G-C3N4 and TiN embedded N-doped graphene for photoelectrochemical reduction of water using sunlight, Adv. Mater. Interfac. 5 (2018) 1.
[18] J.S.J. Hargreaves, Heterogeneous catalysis with metal nitrides, Coord. Chem. Rev. 257 (2013) 2015.
[19] A.B. Dongil, Recent progress on transition metal nitrides nanoparticles as heterogeneous catalysts, Nanomaterials 9 (2019).
[20] B. Abdallah, M. Kakhia, W. Alsadat, W. Zetun, A. Hijazy, Morphology and corrosion behavior study of thin TiN films deposited at different substrates by DC magnetron sputtering, Orbital - Electron. J. Chem. 13 (2021).
[21] B. Abdallah, M. Kakhia, W. Alssadat, M.S. Rihawy, Deposition of Ti6Al4V thin films by DC magnetron sputtering: effect of the current on structural, corrosion and mechanical properties, Iran. J. Sci. Technol. Trans. A-Science 43 (2019) 1957.
[22] I.M. Ismail, B. Abdallah, M. Abou-Kharroub, O. Mrad, XPS and RBS investigation of TiNxOy films prepared by vacuum arc discharge, Nucl. Instrum. Methods Phys. Res. B 271 (2012) 102.
[23] S. Yick, A.T. Murdock, P.J. Martin, D.F. Kennedy, T. Maschmeyer, A. Bendavid, Tuning the plasmonic response of TiN nanoparticles synthesised by the transferred arc plasma technique, Nanoscale 10 (2018) 7566.
[24] R. Bower, D.A.L. Loch, E. Ware, A. Berenov, B. Zou, P.E. Hovsepian, A.P. Ehiasarian, P.K. Petrov, Complementary metal-oxide-semiconductor compatible deposition of nanoscale transition-metal nitride thin films for plasmonic applications, ACS Appl. Mater. Interfaces 12 (2020) 45444.
[25] A. Nardi, M. Turchetti, W.A. Britton, Y. Chen, Y. Yang, L. Dal Negro, K.K. Berggren, P.D. Keathley, Nanoscale refractory doped titanium nitride field emitters, Nanotechnology 32 (2021) 315208.
[26] U. Guler, J.C. Ndukaife, G. V Naik, A.G.A. Nnanna, A. V Kildishev, V.M. Shalaev, A. Boltasseva, Local heating with lithographically fabricated plasmonic titanium nitride nanoparticles, Nano Lett. 13 (2013) 6078.
[27] W. Sun, et al., A map of the inorganic ternary metal nitrides, Nat. Mater. 18 (2019) 732.
[28] L. Mascaretti, T. Barman, B.R. Bricchi, F. Münz, A. Li Bassi, Š. Kment, A. Naldoni, Controlling the plasmonic properties of titanium nitride thin films by radiofrequency substrate biasing in magnetron sputtering, Appl. Surf. Sci. 554 (2021) 149543.
[29] W.-P. Guo, R. Mishra, C.-W. Cheng, B.-H. Wu, L.-J. Chen, M.-T. Lin, S. Gwo, Titanium nitride epitaxial films as a plasmonic material platform: alternative to gold, ACS Photonics 6 (2019) 1848.
[30] R.P. Sugavaneshwar, S. Ishii, T.D. Dao, A. Ohi, T. Nabatame, T. Nagao, Fabrication of highly metallic TiN films by pulsed laser deposition method for plasmonic applications, ACS Photonics 5 (2018) 814.
[31] S. Gbordzoe, R. Kotoka, E. Craven, D. Kumar, F. Wu, J. Narayan, Effect of substrate temperature on the microstructural properties of titanium nitride nanowires grown by pulsed laser deposition, J. Appl. Phys. 116 (2014) 64310.
[32] I.G. Brown, Cathodic Arc deposition of films, Annu. Rev. Mater. Sci. 28 (1998) 243.
[33] B. Abdallah, M. Kakhia, W. Alsadat, W. Zetun, A. Hijazy, Morphology and corrosion behavior study of thin TiN films deposited at different substrates by DC magnetron sputtering, Orbital - Electron. J. Chem. 13 (2021).
[34] B. Abdallah, M. Kakhia, W. Alssadat, M.S. Rihawy, Deposition of Ti6Al4V thin films by DC magnetron sputtering: effect of the current on structural, corrosion and mechanical properties, Iran. J. Sci. Technol. Trans. A-Science 43 (2019) 1957.
[35] B. Abdallah, M. Kakhia, W. Alsadat, Deposition of TiN and TiAlVN thin films by DC magnetron sputtering, International Journal of Structural Integrity 11 (2019) 819.
[36] Y.B. Gerbig, C.A. Michaels, R.F. Cook, In situ observations of Berkovich indentation induced phase transitions in crystalline silicon films, Scripta Mater. 120 (2016) 19.
[37] G. Han, K.P. Marimuthu, H. Lee, Evaluation of thin film material properties using a deep nanoindentation and ANN, Mater. Des. 221 (2022) 111000.
[38] S.J. Bull, Microstructure and indentation response of TiN coatings: the effect of measurement method, Thin Solid Films 688 (2019) 137452.
[39] S. Park, J.H. Fonseca, K.P. Marimuthu, C. Jeong, S. Lee, H. Lee, Determination of material properties of bulk metallic glass using nanoindentation and artificial neural network, Intermetallics 144 (2022) 107492.
[40] L. Lu, M. Dao, P. Kumar, U. Ramamurty, G.E. Karniadakis, S. Suresh, Extraction of Mechanical Properties of Materials through Deep Learning from Instrumented Indentation, vol 117, Proceedings of the National Academy of Sciences, 2020, p. 7052.

[41] H. Lee, W.Y. Huen, V. Vimonsatit, P. Mendis, An investigation of nanomechanical properties of materials using nanoindentation and artificial neural network, Sci. Rep. 9 (2019) 13189.

[42] H. Chen, H. Peng, L. Cai, Z. Meng, W. Li, Z. Fu, Z. Shen, A novel combined dual-conical indentation model for determining plastic properties of metallic materials, J. Mater. Res. Technol. 20 (2022) 3241.

[43] K.M. Calamba, J. Salamania, M.P.J. Jõesaar, L.J.S. Johnson, R. Boyd, J.F. Pierson, M.A. Sortica, D. Primetzhofer, M. Odén, Effect of nitrogen vacancies on the growth, dislocation structure, and decomposition of single crystal epitaxial (Ti1-XAlx)Ny thin films, Acta Mater. 203 (2021) 116509.

[44] P. Cheng, T. Ye, H. Zeng, J. Ding, Raman spectra investigation on the pressure-induced phase transition in titanium nitride (TiN), AIP Adv. 10 (2020) 045110.

[45] G.M. Oliver, W.C. Pharr, Measurement of hardness and elastic modulus by instrumented indentation: advances in understanding and refinements to methodology, J. Mater. Res. 19 (2004) 3.

[46] D.K. Patel, S.R. Kalidindi, Correlation of spherical nanoindentation stress-strain curves to simple compression stress-strain curves for elastic-plastic isotropic materials using finite element models, Acta Mater. 112 (2016) 295.

[47] K. Bobzin, E. Lugscheider, M. Maes, P. Immich, S. Bolz, Grain size evaluation of pulsed TiAlN nanocomposite coatings for cutting tools, Thin Solid Films 515 (2007) 3681.

[48] Y.H. Cheng, B.K. Tay, S.P. Lau, Electrical properties of TiN films deposited by filtered cathodic vacuum arc, J. Vac. Sci. Technol. B: Microelectronics and Nanometer Structures Processing, Measurement, and Phenomena 20 (2002) 2000.

[49] A. Darvizeh, E. Bazzaz, M. Alitavoli, M. Yarmohammad Tooski, New hybrid approach in obtaining plastic properties by nanoindentation, finite element method and modified dimensional analysis, Journal of Science and Technology of Composites 6 (2019) 451.